Real-Time 3D Reconstruction Based on Single-Photon LiDAR for Underwater Environments

Yifei Chen

Department of Mechanical Engineering, Tsinghua University, Beijing, 100084, China

Keywords: Real-Time 3D Reconstruction, LiDAR, RT3D.

Abstract: This paper compares three real-time 3D reconstruction methods based on single-photon LiDAR technology in underwater environments. Methods include the traditional cross-correlation method, the RT3D method combining highly scalable computational techniques from the computer graphics field with statistical models, and the ensemble method which combines surface detection and distance estimation are all explored. The target was placed around three meters away from the transceiver system, and both were submerged in a 1.8-meter-deep water tank as part of the experimental setup. The transceiver used a picosecond pulse laser source that emitted light at a frequency of 20 MHz with a center wavelength of 532 nm. The results indicate that in static scenarios, as the turbidity of the medium increases, the cross-correlation method exhibited the most significant increase in noise and loss of surface detail; the RT3D method showed less noise increase but more pronounced surface loss; the Ensemble Method overall performed the best. The cross-correlation approach was found to be much faster than the other two ways in dynamic scenes, with the Ensemble approach being marginally slower than the RT3D method, all three methods' processing times reduced as the attenuation length rose. When the attenuation length exceeded 5.5AL, none of the methods could perform 3D reconstruction, but both RT3D and Ensemble Methods could still produce clusters of points.

1 INTRODUCTION

Real-time 3D reconstruction is a popular area of study within the domains computer vision that is used in robot and other automated equipments. 3D reconstruction is known as the process of recreating different aspects of the natural world we are living in into a virtual environment (Ingale 2021). Essentially, it involves capturing the three-dimensional spatial coordinates of every point on the surfaces of objects in real-world scenes. These captured points, embedded with spatial coordinate information, are then depicted within a unified 3D coordinate system using computer simulation software. This process accurately restores the surface contours of all objects within the target environment. When we raise our requirements for 3D reconstruction to achieve real-time processing, it allows users to interact in real-time within the 3D scene, which opens up possibilities for various real-time applications such as real-time medical imaging, critical parameter measurement of high-temperature metal components, AR real-time interaction and mobile robot mapping and navigation (Wollborn et al 2023, Wen et al 2021 & Wang et al

2023). Depending on the method of depth information acquisition, real-time 3D reconstruction techniques could be categorized into the following main types: the active reconstruction and the passive reconstruction. Active 3D reconstruction uses LiDAR such as TOF depth cameras or structured light methods like Microsoft's Kinect camera which sends a predefined signal to the target object and then receives and processes the returned signal to obtain the object's depth information. Passive real-time 3D reconstruction typically requires multiple image captures using cameras. The images are then processed to extract object feature information, which is used to compute the object's three-dimensional coordinates.

In the process of exploration and utilization of marine resources, real-time 3D reconstruction offers profound insights into comprehending and capitalizing in underwater environment. Underwater 3D maps can help monitor coral reefs, record the shapes of Cenotes, and support underwater rescue operations (Williams and Mahon 2004 & Gary et al 2008). However, while real-time 3D reconstruction technology is rapidly advancing due to the influence

of autonomous driving and mobile robot research, underwater 3D reconstruction remains a challenging research problem. This is because water, unlike air, has high electrical conductivity and dielectric constants. Thus, it is not easy to receive GPS signals underwater. Additionally, the scattering and absorption properties of light in water differ from those in air. The presence of suspended particles in water, originating from human or natural phenomena, further attenuates light. (Menna et al 2018). Therefore, it is challenging for cameras to extract sufficient information for subsequent feature point detection, matching, camera motion recovery, and depth and disparity estimation of the 3D scene. The unique physical properties of water also limit the use of light detection and ranging system (LiDAR), a fast and reliable 3D reconstruction method on land, significantly reducing the effective detection range of targets. In order to minimize the interference of the underwater environment, to enhance the real-time accuracy and robustness of underwater 3D reconstruction, more effective sensors and data processing methods are required.

In order to perform 3D reconstruction in water and other complex media, researchers have developed single-photon LiDAR imaging sensors in recent years. Single-photon LiDAR imaging sensor has high surface delineation capabilities and optical sensitivity. The systems are typically based on the Time-of-Flight (ToF) method and Time-Correlated Single Photon Counting (TCSPC) technology. Single-photon LiDAR utilizes short pulse widths and high repetition rate lasers, combined with highly sensitive detectors, to detect and count returned single photons. Using TCSPC technology, single-photon LiDAR is capable of high-resolution 3D single-photon imaging in scattering underwater environments (Maccarone et al 2015). Although there are many advantages using single-photon LiDAR imaging, capturing enough photon events to establish accurate parameter estimates may require a long acquisition time. To further increase the speed of acquiring scene depth data and simplify the optical configuration, researchers have developed the Single-photon avalanche diode (SPAD) for active imaging. A study by A. Maccarone et al. utilized a Complementary Metal Oxide Semiconductor (CMOS) SPAD detector array combined with TCSPC timing electronic components, reaching visualization frame rates of 10Hz in scattering environments with distances up to 6.7AL between the moving target and the systems (Maccarone et al 2019). However, these studies did not achieve real-time imaging systems. One of the main limitations comes from the data

processing segment. The SPAD array's high data rate had a significant impact on data processing since larger data volumes require longer processing times to estimate the intensity and distance data distribution of targets, which reduces the potential for real-time reconstruction.

To further enhance the real-time capabilities of single-photon 3D reconstruction technology, researchers have developed custom computational models implemented on Graphics Processing Units (GPUs). J. Tachella et al. introduced a Real-time 3D algorithm (RT3D) that uses point cloud denoising tools presented priviously in a plug-and-play framework. The RT3D method build fast and robust distance estimation for single-photon LiDAR (Tachella et al 2019). RT3D achieved video rates of 50 Hz with processing times as low as 20 ms. K. Drummond et al. studied the joint surface detection problem of single-photon LiDAR data, with the and depth estimation problem, proposing a 3D reconstruction algorithm based on combined surface detection and distance estimation (Drummond et al 2021). S. Plosz et al. introduced a highly robust, fast single-photon LiDAR 3D reconstruction algorithm and applied it to a pre-collected underwater dataset, and in the environment up to 4.6AL, they achieved 10 milliseconds processing times (Plosz et al 2023). However, these studies did not produce a combined acquisition device and GPU into a comprehensive underwater 3D reconstruction imaging system.

This paper presents the comprehensive underwater 3D reconstruction system proposed by A. Maccarone et al., which is based on the Si-CMOS SPAD detector array and incorporates real-time imaging capabilities with a workstation that is GPU-equipped (Maccarone et al 2023). The discourse further contrasts the performance of the RT3D algorithm with the traditional cross-correlation method and a recently developed method that amalgamates surface detection and distance estimation by Drummond et al. within this experimental framework.

2 METHODS

This section elucidates the fundamental principles of single-photon LiDAR, accompanied by a concise overview of traditional cross-correlation method, the RT3D algorithm and the recently developed algorithms that amalgamate surface detection with distance estimation (Ensemble Method). The RT3D method is restricted to reconstructing one surface per pixel at most to ensure fairness in comparison. This

section will first introduce fundamental principles of single-photon LiDAR, then observation model for the three methods, finally principles of each method.

2.1 Fundamental Principles of Single-Photon Lidar

The detection of a single photon by a single-photon detector is not a deterministic event, but rather a probabilistic one. This probabilistic event is termed PDE, defined as the likelihood of triggering the detector once a photon enters it. In practical engineering applications, for photons of a fixed wavelength, PDE is commonly denoted as η_D.

According to the research on laser echo characteristics by Goodman et al., from the perspective of regular distribution, for specular targets, the number of echo photons reflected by the laser pulse statistically follows a Poisson distribution (Goodman 1965). For rough targets, however, the echo photon events statistically adhere to a negative binomial distribution. That is, for specular targets, within the sampling time,

$$f(k|E) = \frac{\left(\frac{\eta_D E}{h\nu}\right)^k}{k!} exp\left(\frac{\eta_D E}{h\nu}\right), \qquad (1)$$

where E represents the energy carried by the echo light signal reflected from the specular target, k denotes the number of timing events triggered when the external signal is input to TCSPC, and f signifies the probability density function of the detector receiving the energy of the echo light signal, ν is the frequency of the echo light signal, and h is the Planck constant.

For rough targets, within the sampling time，

$$(k) = \frac{\Gamma(k+M)}{\Gamma(1+k)\Gamma(M)}\left(\frac{M}{N+M}\right)^M \left(\frac{N}{M+N}\right)^k, \qquad (2)$$

where $f(k)$ represents the conditional probability of generating k timing events, Γ is the gamma function, M denotes the degrees of freedom of speckle presented in the echo light signal space, N signifies the average number of photoelectrons within the sampling time. For photon counting lidar employing TCSPC counting, $M \gg N$, the expression for non-specular targets will also converge to the form of a Poisson distribution.

In summary, the Poisson response model of the single-photon detector to photons within the time interval (t_1, t_2) is

$$f(t_1, k, t_2) = \frac{1}{k!}[M(t_2, t_1)]^k exp[-M(t_2, t_1)], \qquad (3)$$

$$M(t_2, t_1) = \int_{t1}^{t2} \frac{P_r}{J_p}(t - \tau)d\tau, \qquad (4)$$

where P_r represents the energy of the echo signal, J_p denotes a single photon's energy.

2.2 Observation Model

This paper establishes the observation model which is based on the research of Legros et al. Think of a series of K temporal frames with P pixels each, with the data linked to every pixel in a frame made up of a collection of reflected photon arrival timings (ToF). It is assumed that in each frame things happen in static scene, and the detection events caused by dark counts and other sources are uniformly distributed. For a known pixel, within a temporal window of width T, the photon ToFs are $y = \{y_k\}_{k=1}^K$, where $y_k \in (0, T)$. At this point, the probability density can be written down function as

$$f(y_k|d, \omega) = wh_0\left(y_k - \frac{2d}{c}\right) + (1 - \omega)U_{(0,T)}(y_k), \qquad (5)$$

where d is the separation between the surface being viewed and the reconstruction imaging system, c represents the median of the speed of light, ω denotes the likelihood that the photons that were released from the laser source, reflected off the target, and then returned to the photon detector are related to the recorded ToF values. It can alternatively be understood as the pixel's signal-to-background ratio (SBR), which is influenced by the background level and target reflectance. h_0 is the normalized instrumental response function (IRF). The background distribution is noted as $U_{(0,T)}$. The joint probability distribution would be

$$f(y|d, \omega) = \prod_k f(y_k|d, \omega) \qquad (6)$$

2.3 Cross-Correlation

Cross-correlation is a common method used in LIDAR ranging. The normalized waveform template is denoted as $N_p(t_k)$, and the measured waveform signal is $N_0(t_k)$. The cross-correlation value of $N_p(t_k)$ and $N_0(t_k)$ at the time slot k is $Cor(t_k)$. Initially, the shorter sequence $N_p(t_k)$ is zero-padded on the left starting point to make the new sequence $N_{pe}(t_k)$ have the same length as BB. The expression for cross-correlation then becomes

$$Cor(t_k) = \sum_{i=1}^M N_{pe}(t_i)N_0(t_i), \qquad (7)$$

where M represents the number of time slots occupied by the measured waveform signal $N_0(t_k)$.

The time slot position corresponding to the maximum value of the cross-correlation $Cor_T(t_k)$ is the approximate location D_i of the target flight time D,

$$D_i = \underset{t_k}{\mathrm{argmax}}[Cor_T(t_k)] \qquad (8)$$

To obtain a more refined distance D, this paper calculates the difference between the centroid P_1 of the waveform $N_{0(t_k)}$ in the interval $[D_i - \frac{P_w}{\tau}, D_i + \frac{P_w}{\tau}]$ and the centroid P_2 of the normalized pulse template $N_p(t_k)$ in the interval $[0 - \frac{P_w}{\tau}, 0 + \frac{P_w}{\tau}]$ for the flight time values,

$$D_0 = \frac{\tau}{2P_W} \sum_{i=D_i - \frac{P_w}{\tau}}^{D_i + \frac{P_w}{\tau}} iN_0(t_i) - \frac{\tau}{2P_W} \sum_{i=-\frac{P_w}{\tau}}^{\frac{P_w}{\tau}} iN_0(t_i - 0) \quad (9)$$

where P_W is the Full Width at Half Maximum (FWHM) pulse width of the echo pulse.

The final distance estimation for the target, denoted as d, can be given by:

$$d = \frac{D_0 c}{2}, \qquad (10)$$

where c represents the speed of light.

3 RT3D

J. Tachella et al. introduced a computational framework, referred to as the RT3D algorithm, which is accomplished by combining highly scalable computational techniques from the computer graphics field with statistical models. The algorithm uses photoactivated localization microscopy (PALM) as the general structure while calculating steps for the proximal gradient on background variables b, blocks of depth variables t, and intensity variables r. Every update starts with a gradient step that looks like equation (6) and is based on the log-likelihood term $g(b, t, r)$. After that, there is a denoising step. Precisely, using spheres as local primitives, the algebraic point set surfaces (APSS) algorithm fits a smooth continuous surface to the point set described by the depth variable t in real-world coordinates. The intensity variable r in real-world coordinates uses a manifold metric defined by the point cloud. All points are processed in parallel, considering local correlations only, and removing points with intensities below a given threshold after the denoising step. The proximal operator for the background variable b is replaced by a denoising technique based on the fast Fourier transform.

3.1 Ensemble Method

The Ensemble Method, as described by Drummond et al., is a Bayesian approach that allows for simultaneous relative distance measurement and surface recognition, quickly delivering conservative prior uncertainty. The method depends on the discretization of ω, which has a limited capacity to accept values. It is possible to reframe the surface detection problem, thanks to this discretization, as a hypothesis testing problem. At the same time, the method redefines the distance estimate problem as a set estimation problem. As a result, this approach is called the Ensemble Method. This approach yields not only a 3D map and a detection map that shows the presence or absence of a surface, but also an uncertainty map that offers confidence indications for the accuracy of the estimated distance, intensity, and background profiles. Here, this paper uses the algorithm with default parameters, such as a value of $M = 30$ for ω and an existence measurement probability of $\omega_0 = 0.05$.

4 RESULTS

The detection objects used for the experiment are illustrated in the figures. Figure 1(a) displays a brass tube connector, while Fig. 1(b) and (c) showcase 3D printed cylindrical objects mounted on a black anodized aluminum breadboard, utilized for the three-dimensional reconstruction experiments of stationary targets (Maccarone et al 2023). The brass connector has an inner diameter of 15mm and exhibits intricate three-dimensional features. In contrast, the 3D-printed rectangular objects have heights of 10mm, 20mm, and 30mm, respectively, and possess simpler three-dimensional characteristics. Figure 1(d) and (e) depict objects used for the three-dimensional reconstruction experiments of moving targets. This object is attached to a 2-meter-long rail via a connector, enabling it to move within a three-dimensional space. The experiment involved submerging the transceiver system and the target object in a 1.8-meter-deep water tank. The target was placed at a distance of about 3 meters. In the experiment, picosecond pulse laser source was used. The central wavelength of the laser source is 532 nm, great and the operating frequency is 20 MHz. The measurements were conducted using the same average optical power as specified in Table 1 (Maccarone et al 2023).
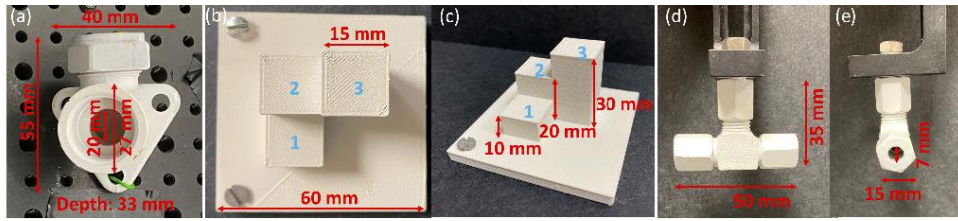
Figure 1: Detection objects.

Table 1: Average optical power.

Attenuation lengths	Concentration of scattering agent	Average optical power
7.5 ± 0.4	0.0046%	52mW
7.1 ± 0.4	0.004%	47mW
5.5 ± 0.4	0.003%	32mW
3.6 ± 0.4	0.002%	22mW
<0.5	0%	0.96 mW

4.1 Static Scenes

Three-dimensional reconstruction of the brass pipe connector was conducted in a static scene. When employing the Ensemble Method, the threshold for the surface detection existence probability is set at $w_0 = 0.05$. Points that have a probability of posterior existence less than 0.5 are excluded, with discarded points being treated as black pixels, setting the pixel value to 0. As illustrated in Fig. 2, during the three-dimensional reconstruction process (Maccarone et al 2023), we aggregated 5000 binary frames. All three 3D reconstruction methods performed well when the attenuation length was less than 0.5AL. However, as the attenuation length increased, images obtained from all three methods exhibited increased noise and surface loss. Among them, the RT3D method showed less noise increment but had more pronounced surface loss. This might be attributed to the smoothing applied to the depth variable t and intensity variable r during point cloud denoising in the RT3D method. The Ensemble Method exhibited a more significant increase in noise compared to RT3D, as there is no denoising step in the Ensemble Method. Overall, the Ensemble Method showed fewer point losses at an attenuation length of 5.5AL and still maintained some denoising effect at 7.1AL. Hence, in static scenes, the Ensemble Method offers superior overall performance in three-dimensional reconstruction.

The Ensemble Method is also employed to perform three-dimensional reconstruction on cylindrical 3D printed objects. Histograms were gated in time, focusing the target within a time window of 400 bins. The finished picture had a gate set between 0 and 50 mm. There are differences in how many binary frames are used to aggregate the histograms. The reconstruction results are shown in Fig. 3 (Maccarone et al 2023). Along the axis, the color represents how far away it is from the transceiver. An arbitrary origin close to the reference target position was used. From the reconstruction results, it is evident that when using the Ensemble Method, the three-dimensional reconstruction's visual quality declines with increasing attenuation length or decreasing aggregated binary frame count, making the identification of target features more challenging.
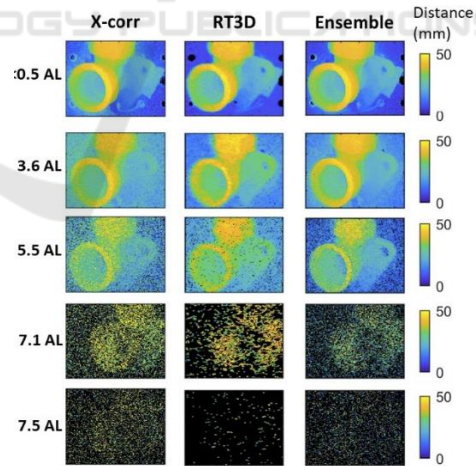

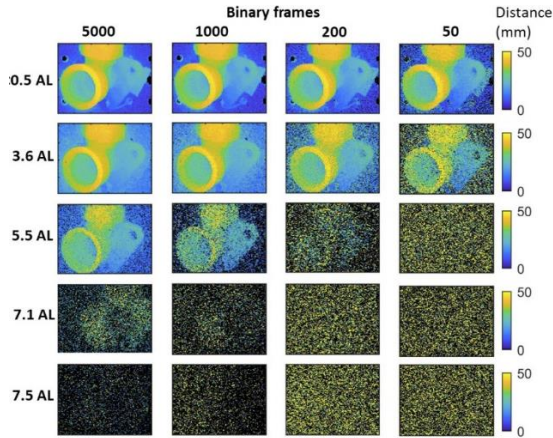Figure 2: 3D profiles at different attenuation lengths using different methods.

Figure 3: Brass pipe connector 3D profiles with different numbers of binary frames using the ensemble method.

4.2 Dynamic Scenes

Table 2: Parallel orientation's average processing time to obtain a single image frame (ms) and standard deviation (in brackets).

Attenuation lengths	Cross-Correlation	RT3D	Ensemble Method
<0.5	1.15(0.11)	34.53(1.25)	32.76(1.21)
0.6	1.42(0.16)	35.34(1.20)	35.78(2.37)
1.4	1.27(0.19)	32.95(1.53)	33.72(1.92)
2.5	1.49(0.24)	34.53(1.38)	37.08(2.58)
3.6	1.20(0.20)	31.34(1.39)	33.05(1.77)
4.8	0.97(0.18)	28.95(1.18)	29.51(1.32)
5.5	0.97(0.13)	29.53(1.38)	30.92(0.91)
6.0	0.93(0.12)	28.54(2.28)	30.12(0.88)
6.6	0.93(0.12)	28.14(1.44)	29.47(0.81)

Table 3: Perpendicular orientation's average processing time to obtain a single image frame (ms) and standard deviation (in brackets).

Attenuation lengths	Cross-Correlation	RT3D	Ensemble Method
<0.5	1.27(0.19)	34.67(1.98)	35.23(2.44)
0.6	1.54(0.19)	36.17(2.80)	37.19(3.11)
1.4	1.35(0.20)	34.83(1.23)	34.51(3.15)
2.5	1.65(0.27)	34.86(1.39)	38.56(2.98)
3.6	1.30(0.15)	32.36(1.74)	34.22(2.28)
4.8	1.02(0.11)	30.74(1.28)	30.07(1.19)
5.5	0.96(0.09)	29.55(1.12)	30.7(0.98)
6.0	0.94(0.09)	28.30(2.77)	20.54(0.9)
6.6	0.91(0.09)	29.46(4.34)	29.7(0.9)

To investigate the characteristics of real-time online three-dimensional reconstruction in dynamic scenes, The T-shaped metal connection made of aluminum is depicted in Fig. 1(d)(e), and it is chosen as the subject of study. The term "parallel direction" refers to the axial direction of the connector's connection hole, which is parallel to the line of sight of the system. Displaying the connector's entire length when oriented perpendicular to the parallel direction, which is called the vertical direction. In the dynamic scene, the experiment aggregated 50 binary frames to generate histograms. Gates were used to control the histograms, focusing the target within a time window of 400 bins. Each pixel was processed in parallel using a GPU to ensure the real-time nature of the 3D reconstruction.

Experiments were conducted using the Cross-Correlation, Ensemble Method, and RT3D methods, with the results presented in Tables 2 and 3 (Maccarone et al 2023). When employing the Ensemble Method, a discrete set of w values, $M = 10$, was chosen. The code was constructed in a modular fashion and delegated to three separate GPU cores for processing. The first step involved obtaining the posterior probability distribution values, followed by normalization, and finally, the results were derived.

The processing time average for a single image frame obtained in the parallel orientation is shown in Table 2, and the processing time average for a single image frame obtained in the vertical orientation is shown in Table 3. The standard deviations for different attenuation lengths are provided in parentheses. As evident from the tables, the processing time for each method decreases with the increase in attenuation length. The cross-correlation method has a significantly greater processing speed than the other two methods. The ensemble method's processing time is slightly slower than that of the RT3D method. Thus, when the attenuation length grows, photons are scattered more widely, which leads to a decrease in the number of returned photons. Consequently, the generated histograms are sparser, leading to reduced processing times.

The results of three-dimensional reconstruction in clear water and target systems with different attenuation lengths are presented in Fig. 4 (Maccarone et al 2023). When the attenuation length exceeds 5.5AL, the target becomes unrecognizable, but clusters of points can still be obtained. This indicates that these methods cannot perform three-dimensional reconstruction in environments with high scattering levels, but they can still track targets. On the other hand, as is shown in Fig. 5 (Maccarone et al 2023), the Cross-Correlation method can be used in low-scattering environments, but it is unable to recognize or detect targets in high-scattering environments.
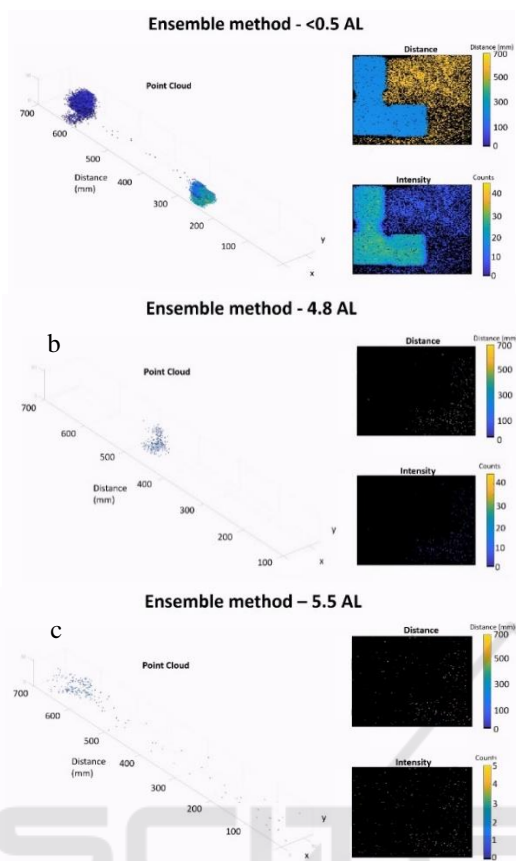
a

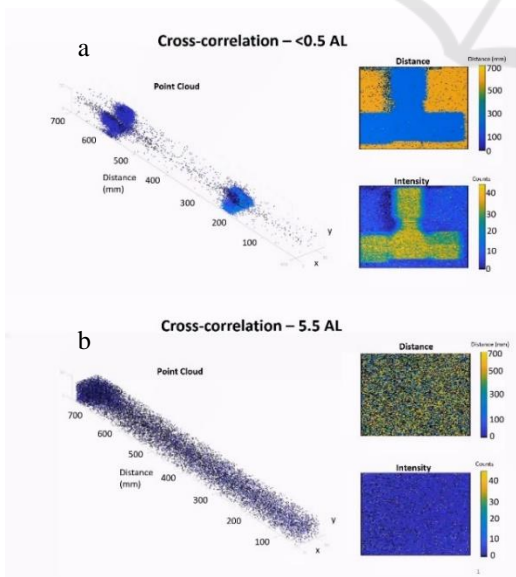Figure 4: 3D real-time profiles at different attenuation lengths using ensemble method.

Figure 5: 3D real-time profiles at different attenuation lengths using cross-correlation method.

5 CONCLUSION

The article presents real-time 3D reconstruction technology underwater based on single-photon LiDAR, comparing the performance of the Ensemble Method, RT3D, and the traditional cross-correlation method in waters of varying turbidity, as proposed by A. Maccarone et al. The experimental results show that in static scenes, all three 3D reconstruction methods perform well in water with low attenuation lengths, but as attenuation increases, they all exhibit more noise and surface loss. Among them, the cross-correlation method performs the worst; the RT3D method has less noise increase but more obvious surface loss; the Ensemble Method loses fewer points at 5.5AL and still has some noise reduction effect at 7.1AL, making it the best performer among the three methods. The cross-correlation approach was found to be much faster than the other two ways in dynamic circumstances, with the Ensemble approach being marginally slower than the RT3D method. All three methods' processing times reduced as the attenuation length rose. When the attenuation length exceeds 5.5AL, none of the methods can perform 3D reconstruction, but the RT3D method and the Ensemble Method can still obtain clusters of points.

REFERENCES

K. Ingale, "Real-time 3D reconstruction techniques applied in dynamic scenes: A systematic literature review," Computer Science Review 39, 100338 (2021).

J. Wollborn, A. Schule, R. D. Sheu, D. C. Shook and C. B. Nyman, "Real-Time multiplanar reconstruction imaging using 3-dimensional transesophageal echocardiography in structural heart interventions," Journal of Cardiothoracic and Vascular Anesthesia, 37(4), 570-581 (2023).

X. Wen, J Wang, G. Zhang and L. Niu, "Three-dimensional morphology and size measurement of high-temperature metal components based on machine vision technology: a review," Sensors, 21(14), 4680 (2021).

W. Wang, B. Joshi, N. Burgdorfer, K. Batsos, A. Q. Li, P. Mordohai and I. M. Rekleitis, "Real-Time Dense 3D Mapping of Underwater Environments", 2023 IEEE International Conference on Robotics and Automation, 5184-5191 (2023).

S. Williams and I. Mahon, "Simultaneous localisation and mapping on the great barrier reef", IEEE International Conference on Robotics and Automation, 2, 1771-1776 (2004).

M. Gary, N. Fairfield, W. C. Stone, D. Wettergreen, G, Kantor and J. M. Sharp, "3D Mapping and Characterization of Sistema Zacatón from DEPTHX

(DE ep P hreatic TH ermal e X plorer)," Sinkholes and the Engineering and Environmental Impacts of Karst, 202-212 (2008).

F. Menna, P. Agrafiotis and A. Georgopoulos, "State of the art and applications in archaeological underwater 3D recording and mapping," Journal of Cultural Heritage, 33, 231-248 (2018).

Maccarone, A. McCarthy, X. Ren, R. E. Warbutrton, A. M. Wallace, J. Moffat, Y, Petillot and G. S. Buller, "Underwater depth imaging using time-correlated single-photon counting, " Optics express, 23(26), 33911-33926 (2015).

Maccarone, F. M. Della Rocca, A. McCarthy, A. McCarthy, R. Henderson and G. S. Buller, "Three-dimensional imaging of stationary and moving targets in turbid underwater environments using a single-photon detector array," Optics express, 27(20), 28437-28456 (2019).

J. Tachella, Y. Altmann, N. Mellado, A. McCarthy, R. Tobin, G. S. Buller, J. Y. Tourneret and S. McLaughlin, "Real-time 3D reconstruction from single-photon lidar data using plug-and-play point cloud denoisers, "Nature communications, 10(1), 4984 (2019).

K. Drummond, S. McLaughlin, Y. Altmann, A. Pawlikowska and R. Lamb, "Joint surface detection and depth estimation from single-photon Lidar data using ensemble estimators," 2021 Sensor Signal Processing for Defence Conference (SSPD), pp. 1-5 (2021).

S. Plosz, A. Maccarone, S. McLaughlin, G. S. Buller and A. Halimi, "Real-Time Reconstruction of 3D Videos From Single-Photon LiDaR Data in the Presence of Obscurants," IEEE Transactions on Computational Imaging, vol. 9, pp. 106-119 (2023).

A. Maccarone, K. Drummond, A. McCarthy and U. K. S. Teinlehner, "Submerged single-photon LiDAR imaging sensor used for real-time 3D scene reconstruction in scattering underwater environments," Optics Express, 31(10), 16690-16708 (2023).

J. W. Goodman, "Some effects of target-induced scintillation on optical radar performance," Proceedings of the IEEE, 53(11), 1688-1700 (1965).

Q. Legros, J. Tachella, R. Tobin, A. McMarthy, S. Meignen, G. S. Buller, Y. Altmann, S, McLayghlin and M. E. Davies, "Robust 3d reconstruction of dynamic scenes from single-photon lidar using beta-divergences," IEEE Transactions on Image Processing, 30, 1716-1727 (2020).